PCCP

Accepted Manuscript

ROYAL SOCIETY OF CHEMISTRY

www.rsc.org/pccp

Atomistic modeling to optimize composition and characterize structure of Ni-Zr-Mo metallic glasses

M.H. Yang, S.N. Li, Y. Li, J.H. Li and B.X. Liu*

Key Laboratory of Advanced Materials (MOE), School of Materials science and Engineering, Tsinghua University, Beijing 100084, China

ABSTRACT

An interatomic potential was constructed for the Ni-Zr-Mo ternary metal system with the newly proposed long-range empirical formulism, which has been verified to be applicable for *fcc*, *hcp* and *bcc* transition metals and their alloys. Applying the constructed potential, molecular dynamics simulations predict a hexagonal composition region within which metallic glass formation is energetically favored. Based on the simulation results, the driving force for amorphous phase formation is derived, and thus an optimized composition is pinpointed to $Ni_{45}Zr_{40}Mo_{15}$, of which the metallic glass could be most stable or easiest obtainable. Further structural analysis indicates that the dominant interconnected clusters for $Ni_{64}Zr_{36-x}Mo_x$ MGs are <0, 0, 12, 0>, <0, 1, 10, 2>, <0, 2, 8, 2> and <0, 3, 6, 4>. Meanwhile, it is found that the appropriate addition of Mo content could not only make a more ordered structure with a higher atomic packing density and a lower energy state, but also improve the glass formation ability of Ni-Zr-Mo alloys. Moreover, inherent hierarchical atomic configurations for ternary Ni-Zr-Mo metallic glasses are clarified via the short-range, medium-range and further in the extended scale of the icosahedral network.

* Corresponding author: dmslbx@tsinghua.edu.cn.

1. Introduction

Owing to their excellent mechanical, physical, and chemical properties, the Ni-Zr alloys, just like Cu-Zr alloys, have been studied extensively as one of the promising candidates for structural and functional materials.[1-6] Besides, the Ni-Zr binary system is a system in which metallic glasses (MGs) can be formed over wide composition ranges. It has been reported that the glassy ribbons were formed in 30-80 at.% Zr by melt-spinning technique and ion beam mixing (IBM) experimental data show a glass formation composition range of 30-65 at.% Zr.[7, 8] Nowadays, many efforts have been devoted to the study of the atomic structures, mechanical properties, electronic properties and dynamic properties of Ni-Zr MGs.[9-11] In contrast, seldom attentions have been paid on the addition of the elements on the glass formation ability (GFA) of this system. With the addition of appropriate amount of Mo, the stabilization of supercooled liquid and GFA of Fe-based bulk metallic glasses was significantly enhanced, and fully amorphous rods with a diameter of up to 5 mm were produced.[12, 13] It is also found that the micro-addition of Mo seem to be more effective to improve the GFA and corrosion resistance of Cu-based MGs.[14] Therefore, the Ni-Zr-Mo ternary system is selected for investigation in the present work. We aim to study the effects of the Mo addition on the metallic glass formation and atomic structure of the Ni-Zr binary system.

In practice, researchers frequently use some technical parameters to describe the GFA of an alloy or to compare the GFAs of two alloys. A few simple criteria or parameters have been proposed based on the characteristic temperatures, such as the

reduced glass transition temperature T_{rg} (=T_g/T_m),[15] the supercooled liquid region ΔT_{xg} (=T_x-T_g),[16] and the new parameter γ=$T_x/(T_g+T_m)$,[17] where T_g, T_m and T_x are the glass transition temperature, melting temperature and onset crystallization temperature, respectively. However, these criteria are not convenient for predicting the GFA, as the essential temperature parameters require rather complicated and time-consuming experimental tests and measurements. Therefore, it is necessary to propose a reliable model that can be used to predict the metallic glass formation compositions *a priori*, or at least provide estimates for such compositions to guide the experiments. In principle, the GFA of an alloy not only depends on the applied producing techniques, but also is governed by the intrinsic characteristics of the system. From a theoretical perspective, the interatomic potential of an alloy system describes the major interatomic interactions among all the atoms involved in the system, and thus governs the intrinsic characteristic of the alloy system, such as GFA. It would be an appropriate choice to clarify the underlying physics of an alloy system from its interatomic potential. Once a realistic interatomic potential is constructed, many physical properties and behaviors, including the atomic configurations of the system, could be derived through relevant computations and simulations.[18] In the present work, we take the interatomic potential as the starting base to develop a model capable of clarifying the metallic glass formation and predicting the favored and even optimized compositions for obtaining the desired MGs.

Meanwhile, glass formation, as well as many other physical and mechanical properties of MGs, is believed to correlate to the internal atomic structure.[19] It has

been widely accepted that icosahedral or icosahedra-like short-range orders (SROs) are the basic building block in MGs as demonstrated by computer simulations and experimental studies. For instance, the $Ni_{64}Zr_{36}$ MGs with a large variety of polyhedra, ~25% of which have icosahedra-like structures, are established to be characterized by pronounced topological and chemical short-range atomic ordering with preferred Ni-Zr bonding.[20, 21] However, how the SROs of this alloy distribute and interconnected with one another in the three-dimensional (3D) space remains a mystery and much effort should be made to unravel the higher hierarchy of order, *i.e.*, medium-range order (MRO).[22-25] Recent studies confirm that the characteristics of MRO clusters dictate the stability and mechanical properties of monolithic MGs, which have shed new lights on our understanding of structural features at this length scale.[26] Owing to the complexity and diversity of internal interactions in alloy systems, the packing details in the MRO can be probing into an even higher hierarchical level, *i.e.*, the percolation of structural order throughout the entire sample. For instance, it is revealed that the interpenetrating linkages of icosahedra in Cu-Zr MGs exhibit strong correlation in space and tend to aggregate and form string-like networks.[27, 28] Besides, the icosahedral network formed in Cu-Zr MGs are resistant to shear softening and have high elastic rigidities.[29] Therefore, resolving the characteristics of the spatial network is crucial to provide an explicit picture of the hierarchical structure in MGs and more significantly, to further clarify the structure-property relationships.[30]

Atomistic simulations, including Molecular Dynamics (MD) and Monte Carlo (MC), are applied in the present study. The paper proceeds as follows: (I) a new

long-range *n*-body potential was first constructed for the Ni-Zr-Mo ternary system; (II) based on the interatomic potential, a series of MD and MC simulations were conducted to investigate the glass formation region (GFR) and the optimal compositions for the Ni-Zr-Mo system; (III) the characteristics of hierarchical atomic structure were quantitatively assessed in terms of their connectivity and rigidity; (IV) effects of the Mo addition on the metallic glass formation of the Ni-Zr system were further discussed from the atomic structure perspective.

2. Construction of Ni-Zr-Mo interatomic potential

As we all know, the interatomic potential plays a vitally important role in the atomic simulation. Consequently, a variety of empirical *n*-body potentials have been developed, *e.g.*, the *n*-body potential developed by Finnis and Sinclair,[31] the so-called tight-biding second-moment-approximation (TB-SMA) potential developed by Tomanek *et al.*,[32] and the modified embedded-atom method (MEAM) potential developed by Baskes *et al.*[33] Despite the fact that these potentials have achieved considerable success in the study of bulk, surface, and cluster properties of metals, they have some limitations or drawbacks in the application. For these empirical potentials, cutoff radiuses are commonly adopted and the interaction between atoms is neglected if their distance is larger than the cutoff radius. With a short-range cutoff less than the third nearest-neighbor distance, the potentials could save computer time in large-scale simulations.[34] However, they frequently encounter the unavoidable structural stability problem, *i.e.*, they always predict the same energy for *fcc* and ideal *hcp* structures.

Recently, Dai and Li [35] proposed a new long-range empirical potential for *bcc* and *fcc* metals, and the potential has been extended for *hcp* metals. The proposed potential could distinguish the energy differences between stable and hypothetic structures of *bcc*, *fcc* and *hcp* metals. In particular, it can distinguish the energy difference between the *fcc* and *hcp* structures. Moreover, the total energy and force derived from the proposed potential could keep continuous and smooth in the entire calculation range. Thus, it can properly resolve the cutoff problem without a truncation function.

According to the potential, the potential energy E_i of atom i can be calculated as follows:

$$E_i = \frac{1}{2}\sum_{j\neq i} V(r_{ij}) - \sqrt{\sum_{j\neq i}\phi(r_{ij})}, \tag{1}$$

where the whole second term of *Eq.* 1 is the cohesive part and r_{ij} is the distance between atoms i and j of the system. $V(r_{ij})$ is the pair part and $\phi(r_{ij})$ is the electron density part. These items can be expressed as follows:

$$V(r_{ij}) = (1 - r_{ij}/r_{c1})^m (c_0 + c_1 r_{ij} + c_2 r_{ij}^2 + c_3 r_{ij}^3 + c_4 r_{ij}^4), 0 < r_{ij} \le r_{c1}, \tag{2}$$

$$\phi(r_{ij}) = \alpha^2 (1 - r_{ij}/r_{c2})^n, 0 < r_{ij} \le r_{c2}, \tag{3}$$

where r_{c1} and r_{c2} are the cutoff radii for pair part and electron density part, respectively. The exponent m and n are two integers and adjustable according to the specific metals; α and c_i are the potential parameters to be determined by fitting procedure.

Concerning the interactions between atoms, there should be six sets of potential parameters in the Ni-Zr-Mo ternary system, *i.e.*, three sets for the interactions of pure

metal Ni-Ni, Zr-Zr and Mo-Mo, and three sets for the cross interactions of Ni-Zr, Ni-Mo and Zr-Mo. Generally, the potential parameters of Ni-Ni, Zr-Zr and Mo-Mo were determined by fitting to the basic physical properties, such as the cohesive energies, lattice constants, bulk moduli and elastic constants of pure metals Ni, Zr, Mo.[36, 37] For the cross interactions of Ni-Zr, Ni-Mo and Zr-Mo, they were determined by fitting to the basic physical properties of the intermetallic compounds with various structures and compositions. In order to acquire enough physical properties of the related compounds, *ab initio* calculations were performed by using the Cambridge serial total energy package (CASTEP) in Materials Studio.[38, 39] In the present study, the exchange and correlation items were described by the generalized-gradient approximation (GGA) of Perdew and Wang (PW91),[40] and the ion-electron interactions were treated by the projector augmented wave (PAW) method.[41] The cutoff energy was chosen to be 700.0 eV, and the Brillouin-zone was sampled using the Monkhorst-Pack method [42] with nearly constant *k*-point densities for each calculation.

Now we present the detailed fitting results of the Ni-Zr-Mo interatomic potential. The six sets of potential parameters [43] are summarized in Table 1. As shown in Table 2, it lists the relative stabilities of pure Ni, Zr, and Mo in *bcc*, *fcc*, and *hcp*. It can be seen that the potential derived lattice constants, cohesive energies, and elastic modulus of Ni, Zr, and Mo match well with their experimental values.[36, 37] For the hypothetic structures of Ni, Zr, and Mo, the lattice constants, bulk modulus, and the cohesive energies derived by empirical potential are also close to the results of *ab initio*

calculations, proving the validity of the constructed interatomic potential. Tables 3 and 4 show the lattice constants, formation energies, and bulk moduli of related intermetallic compounds in the Ni-Zr, Ni-Mo and Zr-Mo binary systems derived from potential. Comparing with the experimental data[44-47] and *ab initio* calculations, it can be seen that the physical properties obtained from the interatomic potential are consistent with those obtained from the experiments or *ab initio* calculations, confirming that the constructed potentials could well derive the structure and energy of these compounds in the systems.

To further evaluate the validity of the constructed potential, another approach is to check whether the potential can describe atomic interactions under non-equilibrium states. Therefore, we obtain the equation of state (EOS) from the constructed potential and then compared it with the frequently used EOS in this field, *i.e.*, Rose Equation, which has been proved to be universal for most categories of solids.[48] Fig. 1 plots the pair parts, the cohesive parts and the potential energies as a function of the lattice constants calculated from the constructed potential, and the corresponding Rose Equations for Ni, Zr, Mo, B2 NiZr, B2 NiMo, B2 ZrMo, $L1_2$ $NiZr_3$, $L1_2$ Ni_3Mo and $L1_2$ Zr_3Mo. One can see that the pair parts, cohesive parts and the potential energy of these intermetallic compounds keep smooth and continuous in the entire range, and the EOS derived from the proposed potential agree well with the corresponding Rose Equation. Meanwhile, there are not any discontinuities in energy calculated from the constructed potential for the related compounds, which can avoid unphysical behavior in MD and MC simulations. It follows that the newly constructed long-range

empirical potential can reasonably describe the atomic interactions of the Ni-Zr-Mo system even far from the equilibrium state, thus providing additional evidence that the constructed potentials can be related to the structure and energy of the system.

3. Metallic glass formation for Ni-Zr-Mo system

3.1. Atomic simulation methods

Since the process of producing metallic glasses is always a far-away equilibrium process, the complicated phase can hardly nucleate or grow due to the extremely restricted kinetic condition. It follows that the phase competing against the amorphous phase is the solid solution with one of the three simple structures, *i.e.*, *fcc*, *hcp*, or *bcc*. This viewpoint has been supported by a large number of research results from both experimental and theoretical aspects.[19] As a result, the issue related to glass-formation region of Ni-Zr-Mo system is transformed to an issue of comparing the relative stability of the solid solution to its disorder counterpart, *i.e.*, amorphous alloy, as a function of alloy compositions.

According to the constructed Ni-Zr-Mo potential, a series of MD simulations were implemented using Large-scale Atomic/Molecular Massively Parallel Simulator (LAMMPS) packages[49] to study the relative stabilities of Ni-Zr-Mo solid solutions versus their amorphous counterparts within the entire composition region of the system. As the stable crystalline structures of Ni, Zr and Mo are *fcc*, *hcp* and *bcc*, respectively, three types of solid solution models, *i.e.*, the *fcc*, *hcp* and *bcc* solid solution models, were constructed based on the main component of the alloy composition. For both *fcc* and *bcc* models, the [100], [010] and [001] crystalline directions are parallel to the *x*, *y* and *z* axes, respectively, while for the *hcp* model, the

[100], [120] and [001] crystalline directions are parallel to the *x*, *y* and *z* axes. Periodic boundary conditions were adopted in the three directions. The *fcc*, *bcc* and *hcp* solid solution models consist of 6912 (12×12×12×4) atoms, 3456 (12×12×12×2) atoms and 4000 (10×10×10×4) atoms, respectively. Meanwhile, we varied *x* and *y* with a composition interval of 5% to construct the $Ni_xZr_yMo_{1-x-y}$ solid solution models over the entire composition triangle of the system. In setting the solid solution models, the solute atoms were created by random substitution of a certain number of solvent atoms to obtain a desired concentration. MD simulation was performed in the framework of an isothermal-isobaric ensemble with a time step of 5 femtoseconds. The Nose-Hoover thermostat and barostat were implemented to control the temperature and pressure, respectively. The simulation proceeded at 300 K and 0 Pa for 1 million time steps to achieve a stable state.

In addition to the MD simulation, a sequence of MC simulation was conducted to calculate the formation enthalpy of the solid solutions. The solid solution models were set up in the same way as in MD simulations, and the periodic boundary conditions were adopted in the three directions. MC simulations were performed at 300K and zero pressure in the isothermal-isobaric ensemble. During MC simulations, there are two types of "moves": atom displacement and box deformation. For atom displacement, the simulation system can be treated as a canonical ensemble at constant NVT, *i.e.*, shape and volume of box are fixed. For box deformation, the fraction coordinates of atoms in the box are fixed. Concerning the details of the construction of the MC isothermal-isobaric ensemble, the readers can refer to the

recent published paper.[50]

The structural transitions in solid state models are monitored by the structure factor $S(q)$, which is commonly recognized to provide a firm evidence for the formation of an amorphous phase. The $S(q)$ can be calculated by[51]

$$S(q) = \frac{1}{N}\left\langle \left| \sum_{k=1}^{N} b_k \exp\left(i\vec{q}\cdot\vec{r_k}\right) \right|^2 \right\rangle, \quad (4)$$

where $i = \sqrt{-1}$, N is the number of atoms, and $\vec{q}$ is scattering vector. b_k and $\vec{r_k}$ are the scattering length and position vector of atom k, respectively. One notes that the $S(q)$ calculated by *Eq.* (4) is not normalized. Besides, the structures of the alloys were analyzed using the three-dimensional (3-D) atomic configurations and Voronoi tessellation methods.[52]

3.2. Glass formation region of Ni-Zr-Mo system

We now present the simulation results of the Ni-Zr-Mo system. After adequate MD time steps at a given temperature, the structures of simulation models generally exhibit two states: a crystalline state and an amorphous state. We take two alloys, *i.e.*, $Ni_{90}Zr_5Mo_5$ and $Ni_{64}Zr_{36}$, in the Ni-rich corner as examples. The structure factor $S(q)$ and the projections of the atomic positions for these two alloys are presented in Fig. 2. From Fig. 2 (a), one can see that the $S(q)$ curve of the $Ni_{90}Zr_5Mo_5$ shows apparent crystalline peaks, exhibiting a long-range ordered feature, as is evidenced by the atomic position projection in Fig. 2 (b). For $Ni_{64}Zr_{36}$, all the crystalline peaks in the long distance have smeared out and disappeared in Fig.2 (c), exhibiting a short-range order and long-range disorder feature. For comparison, the total structure factor $S(q)$ of $Ni_{64}Zr_{36}$ measured by XRD is also shown in Fig.2 (c),[21] indicating that the

prediction of the metallic glass formation by MD simulations is valid and believable. The atomic position projection of $Ni_{64}Zr_{36}$ is demonstrated in Fig. 2 (d), in which the original crystalline lattice has spontaneously collapsed and turned into a completely amorphous state. It suggested that when the solute concentration was low, the solid solution could keep its crystalline lattice. With increasing the solute concentration, the crystalline lattice of the solid solution would be severely distorted, and once the solute concentration exceeded a critical value, the crystalline lattice of the solid solution would collapse and turn into a disordered state. Therefore, the underlying physical process of the solid-state crystal-to-amorphous transition is the crystalline lattice collapsing of the solid solution when the solute concentration exceeds the critical solid solubility.

Considering the structural factor $S(q)$ and atomic position projections of each specific alloy, the Ni-Zr-Mo composition triangle is divided into four regions by three critical solid solubility lines, and the metallic glass forming composition diagram is constructed in Fig. 3. When an alloy composition is situated beyond the lines AB, CD, or EF and moving towards one of the three corners, the solid solution structures can remain stable, and these three corner regions are consequently classified as the crystalline regions. When the composition of the alloy moves from the lines AB, CD, and EF towards the central hexagonal region enclosed by ABCDEF, the solid solution structure becomes unstable and would collapse into a disordered state, giving rise to the formation of the amorphous phase. This region is therefore defined as the amorphous region, *i.e.*, the GFR of the Ni-Zr-Mo system. To validate the amorphous

region in Fig. 3, it is of great importance to compare the predicted GFR of the Ni-Zr-Mo system with the thermodynamic predictions and experimental observations. From a thermodynamic viewpoint, the glass formation region of the Ni-Zr-Mo system was predicted under the framework of the Mediema's model and Alonso's method.[53] The GFR predicted by thermodynamics mostly overlaps the predicted region in the present work, indicating that the Ni-Zr-Mo system is a readily glass-forming system. Meanwhile, various experimental results were collected and marked by different symbols, which mostly fall within the hexagonal region. For the Ni-Mo system, the glass formation range of 25-75 at.% Mo acquired by solid-state reaction (SSR)[54] shows a good accordance with that of 25-68 at.% Mo predicted by MD simulations. For the Ni-Zr system, the mechanical alloying (MA) experiments show a glass formation range of 24-83 at.% Ni,[55] and the glass formation range in MD simulations is determined to be within 20-80 at.% Ni, proving the consistence with the composition range calculated in other works. Besides, ternary Ni-Zr-Mo MGs, *i.e.*, $(NiZr)_{100-x}Mo_x$ along the HG line, could be synthesized by IBM as well, of which the compositions marked by red triangles are all located within the shaded area (GFR). From the discussion above, both the thermodynamic and experimental observations suggest that the predictions by MD simulations for the Ni-Zr-Mo system are quite reasonable.

3.3. Optimization of glass formation compositions

According to the MD simulation results, one can conveniently predict the possibility of metallic glass formation in the Ni-Zr-Mo system at a given composition.

Nevertheless, there are still issues related to evaluating the GFA of Ni-Zr-Mo alloys at different compositions, and pinpoint the optimized alloy composition with the highest GFA in the glass formation region. From a thermodynamics viewpoint, the formation enthalpy difference between the amorphous phase and the solid solution could serve as the driving force for amorphization. One can evaluate the GFA of the Ni-Zr-Mo system by calculating the driving force for amorphization at a given alloy composition, *i.e.*, the larger the driving force, the higher the GFA and the easier the amorphous alloys can be formed.

Assume that E_{am} is the energy per atom of the $Ni_xZr_yMo_{1-x-y}$ amorphous phase and E_{Ni}, E_{Zr}, and E_{Mo} are the lattice energies[36, 37] of Ni, Zr, and Mo atoms in ground state, respectively. The formation enthalpy for the amorphous phase ΔH^{am}, which have been calculated in the MD simulations, can be expressed by

$$\Delta H^{\mathrm{am}} = E_{\mathrm{am}} - [xE_{\mathrm{Ni}} + yE_{\mathrm{Zr}} + (1-x-y)E_{\mathrm{Mo}}], \quad (5)$$

Meanwhile, an efficient and relevant MC simulations were performed to compute the formation energy of the solid solutions, *i.e.*, $\Delta H^{\mathrm{s.s}}$. Assume that E_{min} is the minimum energy per atom of the $Ni_xZr_yMo_{1-x-y}$ solid solutions, and the formation enthalpy $\Delta H^{\mathrm{s.s}}$ of the $Ni_xZr_yMo_{1-x-y}$ solid solutions can then be expressed by

$$\Delta H^{\mathrm{s.s}} = E_{\mathrm{min}} - [xE_{\mathrm{Ni}} + yE_{\mathrm{Zr}} + (1-x-y)E_{\mathrm{Mo}}]. \quad (6)$$

Therefore, the formation enthalpy difference between the amorphous phase and the solid solution can be expressed by

$$\Delta H^{\mathrm{am-s.s}} = \Delta E_{\mathrm{am\text{-}s.s}} = E_{\mathrm{am}} - E_{\mathrm{min}}, \quad (7)$$

where the $\Delta H^{\mathrm{am-s.s}}$ is defined as the driving force for amorphization .

Based on the results from the MD and MC simulations, the contour map of the amorphization driving force for Ni-Zr-Mo system is plotted in Fig. 4(a), as well as the driving force for the $(NiZr)_{100-x}Mo_x$ alloys along the HG line is shown in Fig. 4(b). From the Fig. 4(a), the $\Delta E_{am\text{-}s.s}$ is negative over the whole GFR region, indicating that the energy of the amorphous phase is lower than that of the solid solution, thus formation of the amorphous phase is energetically favored. Besides, the larger the energy difference, the stronger the driving force for glass formation. Further inspecting Fig. 4(a), it can be found that the alloy composition represented by red dots features a lower $\Delta E_{am\text{-}s.s}$ than any other composition regions, implying that the driving forces for amorphization are stronger. Within the red dot region, the composition of $Ni_{45}Zr_{40}Mo_{15}$ represented by a black pentagram is characterized with the maximum amorphization driving force, *i.e.*, the optimized composition, which is close to the optimized composition $Ni_{48}Zr_{48}Mo_4$ obtained from thermodynamics.[53] Therefore, the $Ni_{45}Zr_{40}Mo_{15}$ as well as vicinity compositions could be more thermally stable than other alloys in the system, providing an appropriate approach to design alloy compositions for producing Ni-Zr-Mo MGs.

4. Atomic structure of Ni-Zr-Mo metallic glasses

4.1. Voronoi tessellation analysis

It is well known that the Ni-Zr binary alloy system is a typical compound forming system, and much effort have been paid on the atomic structure of the Ni-Zr system from experimental and simulation studies. In order to study the effects of Mo on the atomic configurations of Ni-Zr system, $Ni_{64}Zr_{36}$, $Ni_{64}Zr_{18}Mo_{18}$ and $Ni_{64}Mo_{36}$

MGs are taken as an example. The coordination polyhedra of the $Ni_{64}Zr_{36}$, $Ni_{64}Zr_{18}Mo_{18}$ and $Ni_{64}Mo_{36}$ MGs were analyzed by means of the Voronoi tessellation method, which is used to designate the characteristics of the local environments in the amorphous phase. The cell faces with smaller than 5% of the average face area would be neglected to minimize the degeneracy problem and the effects of thermal vibration. The total and partial coordination number (CN) distributions of the obtained $Ni_{64}Zr_{36}$, $Ni_{64}Zr_{18}Mo_{18}$ and $Ni_{64}Mo_{36}$ MGs are presented in Fig. 5(a), (b) and (c), respectively. One can see that the polyhedra with CN=12, CN=13 and CN=14 are dominant in all of MGs. Further inspecting the figure, one can see that the Ni atoms are mainly surrounded by CN=12 and 13, whereas the dominating polyhedra of the Zr and Mo atoms are CN=14 and 15. Because Ni has smaller atomic radii than Zr and Mo, the predominant short-range local packing unit of Ni should have smaller coordination atoms than those of Zr and Mo. Consequently, most of the coordination polyhedrons with CN less than 13 are almost Ni-centered, while most of those with CN larger than 14 are Zr and Mo centered.

To deduce the details of the atomic configurations, the fractions of the most frequent coordination polyhedra are plotted in Fig. 5(d), (e) and (f). For the $Ni_{64}Zr_{36}$ MGs, the dominant polyhedra around Zr and Ni atoms are shown in Fig. 5(d). Around Ni atoms, the dominant polyhedra are indexed as <0, 0, 12, 0>, <0, 1, 10, 2>, <0, 2, 8, 2>, <0, 2, 8, 4> and <0, 3, 6, 4>, which are consistent with the previously reported by reverse Monte-Carlo (RMC) simulation data.[21] With the Mo concentration increasing to 18 %, it can be seen from Fig. 5(e) that the prevailing coordination polyhedra are

indexed as <0, 0, 12, 0>, <0, 1, 10, 2>, <0, 2, 8, 2> and <0, 3, 6, 4>, indicating the same dominant interconnected clusters with the $Ni_{64}Zr_{36}$ MGs. Although $Ni_{64}Zr_{18}Mo_{18}$ contains equal amounts of Zr and Mo, the Voronoi polyhedral types around Zr and Mo atoms are a little different: the Zr-centered or Mo-centered clusters prefer <0, 1, 10, 4>, <0, 2, 8, 5> and <0, 1, 10, 5>, while the fraction of Zr-centered clusters are larger than that of Mo-centered. With the Mo concentration increasing to 36 %, one can see from Fig. 5(f) that the cluster <0, 3, 6, 4> occupy the largest proportion in all of Voronoi polyhedra, while the population of the <0, 0, 12, 0> cluster decreases to 4.98 % by completely replacing Zr with Mo in $Ni_{64}Zr_{36-x}Mo_x$ MGs.

Inspecting the distribution of Voronoi polyhedra in the $Ni_{64}Zr_{36}$, $Ni_{64}Zr_{18}Mo_{18}$ and $Ni_{64}Mo_{36}$ MGs, it is found that the dominant interconnected clusters are <0, 0, 12, 0>, <0, 1, 10, 2>, <0, 2, 8, 2> and <0, 3, 6, 4>, considered as icosahedral or icosahedral-like. It is known that icosahedral or icosahedral-like polyhedra play an important role to stabilize the structure of metal-metal amorphous alloys because of the efficient atomic packing and energy minimization.[56] Recently, Wu *et al.*[57] analyzed the cluster energy for different kinds of local clusters and found that the <0, 0, 12, 0>, <0, 1, 10, 2>, <0, 2, 8, 2> and <0, 3, 6, 4> clusters have lower energies than other icosahedral-like clusters and the <0, 0, 12, 0> cluster is the most stable structure in MGs. As shown in Fig. 6, it lists the population of the dominant interconnected clusters <0, 0, 12, 0>, <0, 1, 10, 2>, <0, 2, 8, 2> and <0, 3, 6, 4> in $Ni_{64}Zr_{36-x}Mo_x$ MGs. It can be seen that the population of the clusters <0, 1, 10, 2>, <0, 2, 8, 2>

decreases slowly by adding the Mo concentration, while the population of the cluster <0, 3, 6, 4> increases gradually. It is also found that the population of the <0, 0, 12, 0> cluster firstly increases to the maximum value by replacing Zr with 3 % Mo, and then decreases with further increasing the Mo content.

4.2. Hierarchical atomic structure of $Ni_{64}Zr_{64}$ and *$Ni_{64}Zr_{18}Mo_{18}$ metallic glasses*

Among the various SROs, the full icosahedron <0, 0, 12, 0> (FI) possesses a high atomic packing density (equivalently low free volume) and five-fold nearest-neighbor bonds, and has been proved to be a favorable building block for good glass formers.[27, 58] As shown in Fig. 7, it lists the distribution of FI and their networking in the atomic configurations for the $Ni_{64}Zr_{36}$ and $Ni_{64}Zr_{18}Mo_{18}$ MGs. The FI overlap and interconnect to neighbor icosahedral clusters by sharing vertex, edge, face, or volume. It can be seen that the cross-linking degree of the icosahedral network is very high in both systems, but the $Ni_{64}Zr_{36}$ system is more strongly interconnected than the $Ni_{64}Zr_{18}Mo_{18}$ system. This icosahedral network stretches in space and could serve as the backbone of the MG structure over an extended range.

Of all the four different icosahedral linking patterns, it is of great interest to explore the respective roles of these linkages in forming the icosahedral network. By analyzing the configuration of the icosahedral network in $Ni_{64}Zr_{36}$ and $Ni_{64}Zr_{18}Mo_{18}$ MGs, the respective fractions of the vertex, edge, face and volume with neighboring icosahedral clusters are calculated and exhibited in Fig. 8. One can see that the four different linking patterns in $Ni_{64}Zr_{36}$ and $Ni_{64}Zr_{18}Mo_{18}$ MGs are almost the same, while the volume linkage in both of MGs covers the most frequent fraction. Since the

volume linkage has been revealed to be the lowest average potential energy and smaller average atomic volume,[27, 59] it makes the icosahedral network not only energetically more favorable, but also structurally more stable than other types of linkage patterns. By this argument, the volume linkage is likely to be the most important type of the four different linkages to form the MRO and beyond. Meanwhile, although the vertex, edge and face linkages are not crucial for connection of the icosahedral network, the interpenetrated network formed would undoubtedly be strengthened by these noninterpenetrating linkages. These noninterpenetrating linkages build connections among the discrete clusters and contribute to the unification of the network, consolidating the structural and energetic stability of the network.[60] As a result, the volume linkage represents the strongest cluster interaction, while the vertex, edge and face linkages behave as relatively weaker interactions. The various cluster interactions contribute collectively to achieve the stabilized and efficient filling of space.[61]

After deciding on the important icosahedral cluster sharing scheme (the volume-sharing linkage), the next characteristic to examine is how well and extensive the volume-sharing linkage is. Each icosahedron participates in the formation of the icosahedral network to various degrees by sharing its volume with different numbers of neighboring icosahedral clusters. The number is defined as the bond number, N, *i.e.*, how many neighbors in the first-coordination shell are also centers of other icosahedra. It follows that a high N for an icosahedron indicates that this icosahedron bonds with many other icosahedra via volume sharing. As shown in Fig. 9(a) and (b), the

population of isolated clusters (N = 0) in $Ni_{64}Zr_{18}Mo_{18}$ is higher, while $Ni_{64}Zr_{36}$ not only has more icosahedra participating in the formation of the icosahedral network, but also has a higher cross-linking degree as evaluated in terms of N. This will make $Ni_{64}Zr_{36}$ a more ordered structure with a higher atomic packing density and lower energy state.[27]

To further illustrate the hierarchical atomic structure in the Ni-Zr-Mo MGs, the configurations in the medium-range, and further in the extended scale of the icosahedral network are displayed in Fig. 10(a) and (b), respectively. The packing mode in the medium-range is exhibited by a supercluster consisting of 73 atoms in Fig. 10(a). There are seven icosahedra highlighted with dashed circles in the super-cluster, *i.e.*, six Ni-centered <0, 0, 12, 0> and one Mo-centered <0, 0, 12, 0>, which are connected with the neighboring icosahedra by vertex, edge, face and volume linkage. For the connection mode of the icosahedral network in the extended scale, a typical cross-linked patch containing 53 icosahedra with different N is extracted from the $Ni_{64}Zr_{18}Mo_{18}$ MGs and exhibited in Fig. 10(b). Only the center atoms of the icosahedra are plotted as points. Due to the lack of long range periodicity of the icosahedra, the spatial distribution of the icosahedra themselves is not uniform, but rather exhibits a large density fluctuation. Furthermore, the formation of the densely packed icosahedral network that extends in the glassy matrix could have a considerable effect on the macroscopic properties of the MGs.[62]

5. Further discussion

In order to study the Mo addition on the metallic glass formation of the Ni-Zr

system more clearly, the driving force of the $(NiZr)_{100-x}Mo_x$ for amorphization is shown in Fig. 4(b). It is found that the driving force of the $(NiZr)_{100-x}Mo_x$ alloys firstly increases gradually by adding appropriate Mo concentration, and then after reaching the peak value, decreases with further increasing the Mo. Once the addition of Mo is higher than 62 at. %, the solid solution could keep its crystalline lattice and no unique amorphous phases would be formed, indicating that the GFR of $(NiZr)_{100-x}Mo_x$ is 0-62 at.% Mo. The above observation is confirmed by the corresponding IBM experimental data in Fig. 3 along the HG. The critical ion-dosages to form uniform amorphous phases in $(NiZr)_{100-x}Mo_x$ (x = 0, 10, 20 and 40) are 1×10^{15}, 3×10^{15}, 5×10^{15}, 7×10^{15} Xe^+/cm^2, respectively, while the ion-dosages should not be less than 7×10^{15} Xe^+/cm^2 to form unique amorphous phase in $(NiZr)_{40}Mo_{60}$.[63] By comparing the driving force calculated by MC simulations, it is found that $(NiZr)_{100-x}Mo_x$ (x = 0, 10, 20 and 40) fall within the predicted glass formation range, suggesting that the prediction agrees well with the experimental results. After the Mo content reaches to 60 at.%, the $(NiZr)_{40}Mo_{60}$ becomes an amorphous-crystalline coexisted composite formed by IBM.[53] From Fig. 3, it can be seen that because the alloy composition of $(NiZr)_{40}Mo_{60}$ is near the critical solid solubility line, unique amorphous phases are not energetically favored to be formed. Therefore, further increasing the content of Mo would deteriorate the GFA.

It is interesting and important to illustrate the Mo addition on the GFA of the Ni-Zr system from the atomic structure perspective. It follows that in the present study, there are two dominating factors for the above phenomenon. On the one hand, the Mo

addition into the Ni-Zr system allows three atomic sizes with different crystalline structures to adjust the coordination polyhedron. This will increase the atomic packing density of the liquid structure and the forming of short-range compositional order in the liquid phase.[64] Besides, as Mo (r_{Mo}= 1.39 Å) has a radius in between those of Ni (r_{Ni} = 1.25 Å) and Zr (r_{Zr}= 1.58 Å), the atomic size ratio, r_{Ni} / r_{Mo}, is 0.892, which is rather close to the ideal icosahedral ratio of 0.902.[65] This would suggest that Mo surrounded by Ni *only* would be the topologically optimal way for full icosahedron packing,[66] and then increase the possibility of comfortable arrangements to reach the full icosahedron. Therefore, the minor addition of Mo could facilitate the population of the icosahedron <0, 0, 12, 0> for $Ni_{64}Zr_{36-x}Mo_x$ MGs. Meanwhile, the heats of mixing (ΔH_{mix}) of the Ni-Mo and Zr-Mo systems are -11 and -9 kJ/mol, respectively. As a result, the negative ΔH_{mix} of Mo with Ni and Zr would drive Mo to scatter in the Ni-Zr matrix. This will enhance the interactions among the constituent elements and stabilize the amorphous phase, *i.e.*, improve the GFA.[67] On the other hand, a negative heat of mixing also favors compound formation, which limits diffusivity, but competes against glass formation. Moreover, the melting point temperature of Mo is 2850 K, which is much higher than that of Zr, *i.e.*, 2125 K. According to Xia *et al.*' s approach,[68] it is found that high melting point temperature leads to higher formation enthalpy of amorphous phase, thus deteriorating the GFA of the alloy. From the discussion above, the appropriate addition of Mo content could improve the GFA of Ni-Zr-Mo alloys, consisting of *fcc*, *hcp* and *bcc* transition metals.

6. Summary

Taking a long-range empirical Ni-Zr-Mo *n*-body potential as the starting base, the MD and MC simulations not only predict an energetically favored hexagonal region, which is defined as the glass formation region, or the quantitative glass formation ability of the system, but also pinpoint the locally optimized composition as nearby $Ni_{45}Zr_{40}Mo_{15}$. Furthermore, the voronoi analysis revealed that the most favored coordination polyhedra for $Ni_{64}Zr_{36-x}Mo_x$ MGs are <0, 0, 12, 0>, <0, 1, 10, 2>, <0, 2, 8, 2> and <0, 3, 6, 4>, while the population of the full icosahedron <0, 0, 12, 0> increases to the maximum value by replacing Zr with 3 % Mo. Meanwhile, it is found that the appropriate addition of Mo content could make a more ordered structure with a higher atomic packing density and a lower energy state, and also improve the GFA of Ni-Zr-Mo alloys. In forming the icosahedral network, interpenetrating linkages, *i.e.*, volume linkages, play a dominant role, while the network is additionally reinforced by vertex, edge and face sharing linkages, thereby consolidating the energetic and structural stability of the network.

Acknowledgment

The authors are grateful for the financial support from the National Natural Science Foundation of China (51131003), the Ministry of Science and Technology of China (973 Program 2011CB606301, 2012CB825700), and the Administration of Tsinghua University.

Figure captions:

Fig. 1. The pair, cohesive and potential energies as a function of the lattice constants and the corresponding Rose Equation for Ni, Mo and Zr; B2 NiZr, NiMo and ZrMo; $L1_2$ $NiZr_3$, Ni_3Mo and Zr_3Mo.

Fig. 2. Structural factors and atomic position projections are for (a, b) the crystalline state ($Ni_{90}Zr_5Mo_5$) and (c, d) the amorphous state ($Ni_{64}Zr_{36}$). Red solid circles are for Ni, blue solid circles for Zr, and yellow solid circles for Mo.

Fig. 3 The glass formation region (shaded area) derived from MD simulations at 300 K with different experimental data for the Ni-Zr-Mo system.

Fig. 4 The driving force for the crystalline-to-amorphous transition of the Ni-Zr-Mo system calculated from MC simulations (a), and the driving force of the $(NiZr)_{100-x}Mo_x$ alloys for amorphization (b).

Fig. 5 The total and partial CN distributions of the obtained MGs: $Ni_{64}Zr_{36}$ (a), $Ni_{64}Zr_{18}Mo_{18}$ (b) and $Ni_{64}Mo_{36}$ (c). Fractions of the most frequent coordination polyhedra of the obtained MGs: $Ni_{64}Zr_{36}$ (d), $Ni_{64}Zr_{18}Mo_{18}$ (e) and $Ni_{64}Mo_{36}$ (f).

Fig. 6 Variations in the population of the dominant interconnected clusters <0, 0, 12, 0>, <0, 1, 10, 2>, <0, 2, 8, 2> and <0, 3, 6, 4> for $Ni_{64}Zr_{36-x}Mo_x$ MGs.

Fig. 7 Distribution of FI and their networking in the atomic configurations for the $Ni_{64}Zr_{36}$ and $Ni_{64}Zr_{18}Mo_{18}$ MGs. The degree of connectivity of the FI is obviously higher in (a) for $Ni_{64}Zr_{36}$ than in (b) for $Ni_{64}Zr_{18}Mo_{18}$. For clarity, only the top half of the simulation box is shown in (a) and (b).

Fig. 8 Fractions of the four different linkages formed by sharing the vertex, edge, face and volume with neighboring icosahedra. The representative configurations for the different linking patterns are shown in the insets.

Fig. 9 Variations in (a) the population of various icosahedra and (b) their fractions with different bond numbers in $Ni_{64}Zr_{36}$ and $Ni_{64}Zr_{18}Mo_{18}$. It can be seen that $Ni_{64}Zr_{36}$ has a higher degree of medium-range ordering as characterized by its higher population and higher N.

Fig. 10 Hierarchical atomic structures for $Ni_{64}Zr_{18}Mo_{18}$: (a) a supercluster consisting of 73 atoms, in 7 FI highlighted with dashed circles (six Ni-centered and one Mo-centered). The Ni, Zr, and Mo atoms are colored gray, orange and blue, respectively; (b) the connection mode of the icosahedral network in the extended scale is revealed by a cross-linked patch containing 53 icosahedra with different N. Only the center atoms of the icosahedra are plotted as points.

Table 1 The parameter of the constructed potential for the Ni-Zr-Mo system.

	Ni-Ni [43]	Zr-Zr [43]	Mo-Mo	Ni-Zr [43]	Ni-Mo	Zr-Mo
m	4	4	4	4	4	4
n	6	4	6	5	6	5
r_{c1} (Å)	5.750	6.438	4.618	4.783	5.268	4.944
r_{c2} (Å)	7.172	7.223	6.414	7.385	6.217	5.312
c_0 (eV)	322.065	1353.855	11867.251	331.755	1444.553	1582.121
c_1 (eV/Å)	-391.987	-1453.094	-17112.524	-430.706	-1776.802	-2021.254
c_2 (eV/Å^2)	178.332	586.519	9255.419	254.058	810.354	977.406
c_3 (eV/Å^3)	-36.094	-104.936	-2218.683	-74.642	-161.714	-207.188
c_4 (eV/Å^4)	2.770	7.009	198.426	8.798	11.686	15.759
α (eV)*	5.390	7.830	-11.879	8.343	-3.227	-11.513

*The correct form of function ϕ in the reference 43 is $\phi(r_{ij}) = \alpha^2(1-r_{ij}/r_{c2})^n, 0 < r_{ij} \le r_{c2}$. (1 eV = 1.602×10^{-19} J)

Table 2 The lattice constants (Å), cohesive energies (eV), bulk modulus (Mbar), and elastic constants (Mbar) of Ni, Zr, Mo obtained from experiments[36, 37] or *ab initio* calculations (first lines) and constructed potential (second lines).

	Ni	Ni	Ni	Zr	Zr	Zr	Mo	Mo	Mo
	fcc	*bcc*	*hcp*	*hcp*	*bcc*	*fcc*	*bcc*	*fcc*	*hcp*
a	3.520	2.800	2.485	3.230	3.570	4.527	3.150	4.014	2.760
	3.520	2.810	2.487	3.230	3.615	4.537	3.150	4.199	2.970
c (*hcp*)			4.090	5.150					4.940
			4.112	5.151					4.846
E_c	4.450	4.380	4.425	6.250	6.179	6.213	6.820	6.410	6.390
	4.450	4.378	4.435	6.251	6.188	6.220	6.820	6.551	6.552
B_0	1.860	1.953	1.993	0.954	0.974	0.900	2.598	2.396	2.408
	1.865	1.522	1.696	0.994	1.028	0.790	2.599	1.822	1.823
C_{11}	2.481	1.277	3.381	1.434	1.326	0.895	4.637	1.509	2.310
	2.419	1.233	3.076	1.214	1.062	1.029	4.689	2.806	2.932
C_{12}	1.549	2.291	1.323	0.728	0.799	0.902	1.578	2.840	3.864
	1.588	1.666	1.281	0.595	1.011	0.670	1.555	1.330	1.289
C_{44}	1.242	1.537	0.555	0.320	0.635	0.277	1.092	0.043	0.216
	1.199	1.280	0.480	0.499	0.731	0.386	1.002	0.861	0.783
C_{13}			1.296	0.653					1.502
			0.864	0.784					1.252
C_{33}			3.346	1.648					3.317
			3.099	2.193					2.959

Table 3 Lattice constants (Å), cohesion energies (eV), and bulk moduli (MBar) of B2 and $L1_2$ compounds obtained from the results from experiments or *ab initio* calculations[44-47] (first lines) and constructed potential (second lines).

Compounds	NiZr	Ni_3Zr	$NiZr_3$	NiMo	Ni_3Mo	$NiMo_3$	ZrMo	Zr_3Mo	$ZrMo_3$
Space group	B2	$L1_2$	$L1_2$	B2	$L1_2$	$L1_2$	B2	$L1_2$	$L1_2$
a	3.212	3.759	4.279	2.998	3.647	3.871	3.349	4.379	4.126
	3.162	3.770	4.297	3.044	3.584	3.678	3.284	4.428	4.255
E_c	5.720	5.342	5.803	5.390	4.994	6.150	6.054	6.175	6.196
	5.717	5.344	5.767	5.447	5.060	6.001	6.032	6.172	6.189
B_0	1.422	1.697	1.071	2.328	2.230	2.412	1.491	1.172	1.767
	1.463	1.687	1.267	2.625	2.227	1.316	1.524	1.211	1.754

Table 4 Lattice constants (Å), cohesion energies (eV) and bulk moduli (MBar) of $D0_{19}$, $D1_a$ and $D0_a$ compounds obtained from the results from experiments or *ab initio* calculations[44-47] (first line) and constructed potential (second lines).

Compounds	Ni_3Zr	$NiZr_3$	Ni_3Mo	Ni_3Mo	$NiMo_3$	Ni_4Mo	Zr_3Mo	$ZrMo_3$
Space group	$D0_{19}$	$D0_{19}$	$D0_{19}$	$D0_a$	$D0_{19}$	$D1_a$	$D0_{19}$	$D0_{19}$
a or a, b	5.299	5.960	5.100	5.044,4.250	5.530	5.746	6.180	5.890
	5.325	6.072	5.025	4.996,4.235	5.336	5.740	6.201	5.955
c	4.382	5.137	4.283	4.448	4.415	3.572	4.901	4.813
	4.366	5.006	4.249	4.446	4.337	3.544	4.912	4.850
E_c	5.345	5.764	5.133	5.192	6.098	5.062	6.133	6.198
	5.347	5.764	4.985	5.029	5.924	5.019	6.150	6.196
B_0	1.696	1.049	2.163	2.295	2.325	2.329	1.532	1.855
	1.668	1.230	2.165	2.430	2.157	2.593	1.584	1.637

References:

1. C. Y. Yu, X. J. Liu and C. T. Liu, *Intermetallics*, 2014, **53**, 177-182.
2. A. Shavit and R. A. Riggleman, *Phys. Chem. Chem. Phys.*, 2014, **16**, 10301-10309.
3. N. Takeshi, T. Kazuya and U. Yukichi, *Intermetallics*, 2011, **19**, 511-517.
4. R. Ristic, M. Stubicar and E. Babic, *Philos. Mag.*, 2007, **87**, 5629-5637.
5. A. I. Zaitsev, N. E. Zaitseva, J. P. Alexeeva, S. F. Dunaev and Y. S. Nechaev, *Phys. Chem. Chem. Phys.*, 2003, **5**, 4185-4196.
6. A. I. Zaitsev, N. E. Zaitseva, E. K. Shakhpazov and A. A. Kodentsov, *Phys. Chem. Chem. Phys.*, 2002, **4**, 6047-6058.
7. L. J. Huang, J. R. Ding and H. Li, *J. Appl. Phys.*, 1988, **63**, 2879-2881.
8. Z. Altounian and J. O. Strom-Olsen, *Phys. Rev. B*, 1983, **27**, 4149-4156.
9. M. L. Johnson, N. A. Mauro, A. J. Vogt, M. E. Blodgett, C. Pueblo and K. F. Kelton, *J. Non-Cryst. Solids*, 2014, **405**, 211-218.
10. X. J. Liu, G. L. Chen, X. Hui, T. Liu and Z. P. Lu, *Appl. Phys. Lett.*, 2008, **93**, 11911.
11. Q. W. Yang and T. Zhang, *Chin. Phys. Lett.*, 2006, **23**, 915-918.
12. W. Zhang, X. J. Jia, Y. H. Li and C. F. Fang, *J. Appl. Phys.*, 2014, **115**, 17A-768A.
13. Z. B. Jiao, H. X. Li, Y. Wu, J. E. Gao, S. L. Wang, S. H. Yi and Z. P. Lu, *Sci. China-Phys. Mech. Astron.*, 2010, **53**, 430-434.
14. B. Liu and L. Liu, *Intermetallics*, 2007, **15**, 679-682.
15. D. Turnbull, *Contemp. Phys.*, 1969, **10**, 473-488.
16. A. Inoue, T. Zhang and T. Masumoto, *Mater. Trans., JIM*, 1990, **31**, 177-183.
17. Z. P. Lu and C. T. Liu, *Acta Mater.*, 2002, **50**, 3501-3512.
18. Y. Y. Cui, T. L. Wang, J. H. Li, Y. Dai and B. X. Liu, *Phys. Chem. Chem. Phys.*, 2011, **13**, 4103-4108.
19. Q. Wang, J. H. Li, J. B. Liu and B. X. Liu, *J. Phys. Chem. B*, 2014, **118**, 4442-4449.
20. M. Guerdane, H. Teichler and B. Nestler, *Phys. Rev. Lett.*, 2013, **110**, 86105.
21. I. Kaban, P. Jóvári, V. Kokotin, O. Shuleshova, B. Beuneu, K. Saksl, N. Mattern, J. Eckert and A. L. Greer, *Acta Mater.*, 2013, **61**, 2509-2520.
22. L. Huang, C. Z. Wang, S. G. Hao, M. J. Kramer and K. M. Ho, *Phys. Rev. B*, 2010, **81**, 94118.
23. A. Hirata, P. F. Guan, T. Fujita, Y. Hirotsu, A. Inoue, A. R. Yavari, T. Sakurai and M. Chen, *Nat. Mater.*, 2010, **10**, 28-33.
24. H. W. Sheng, W. K. Luo, F. M. Alamgir, J. M. Bai and E. Ma, *Nature*, 2006, **439**, 419-425.
25. B. J., M. S., K. V., R. U. and F. H., *Phys. Chem. Chem. Phys.*, 2013, **15**, 8470-8479.
26. X. J. Liu, Y. Xu, X. Hui, Z. P. Lu, F. Li, G. L. Chen, J. Lu and C. T. Liu, *Phys. Rev. Lett.*, 2010, **105**, 155501.
27. M. Lee, C. M. Lee, K. R. Lee, E. Ma and J. C. Lee, *Acta Mater.*, 2011, **59**, 159-170.
28. M. Z. Li, C. Wang, S. Hao, M. Kramer and K. Ho, *Phys. Rev. B*, 2009, **80**, 184201.
29. M. Wakeda and Y. Shibutani, *Acta Mater.*, 2010, **58**, 3963-3969.
30. P. S. Salmon and A. Zeidler, *Phys. Chem. Chem. Phys.*, 2013, **15**, 15286-15308.
31. M. W. Finnis and J. E. Sinclair, *Philos. Mag. A*, 1984, **50**, 45-55.
32. D. Tomanek, A. A. Aligia and C. A. Balseiro, *Phys. Rev. B*, 1985, **32**, 5051.
33. M. I. Baskes and R. A. Johnson, *Model. Simul. Mater. Sci. Eng.*, 1994, **2**, 147.
34. R. A. Johnson and D. J. Oh, *J. Mater. Res.*, 1989, **4**, 1195-1201.

35. X. Dai, Y. Kong and J. Li, *Phys. Rev. B*, 2007, **75**, 104101.
36. D. R. Lide and T. J. Bruno, *CRC handbook of chemistry and physics*, CRC press, New York, 2012.
37. C. Kittel and M. P, *Introduction to solid state physics*, Wiley, New York, 1996.
38. S. J. Clark, M. D. Segall, C. J. Pickard, P. J. Hasnip, M. I. Probert, K. Refson and M. C. Payne, *Z. Kristallogr. - Cryst. Mater.*, 2005, **220**, 567-570.
39. M. D. Segall, P. J. D. Lindan, M. J. Probert, C. J. Pickard, P. J. Hasnip and S. J. Clark, *J. Phys.: Condens. Matter.*, 2002, **14**, 2717.
40. J. P. Perdew and Y. Wang, *Phys. Rev. B*, 1992, **46**, 12947-12954.
41. P. E. Blochl, *Phys. Rev. B*, 1994, **50**, 17953-17979.
42. H. J. Monkhorst and J. D. Pack, *Phys. Rev. B*, 1976, **13**, 5188-5192.
43. Y. Dai, J. H. Li and B. X. Liu, *J. Appl. Phys.*, 2011, **109**, 53505-53509.
44. H. Ikehata, N. Nagasako, T. Furuta, A. Fukumoto, K. Miwa and T. Saito, *Phys. Rev. B*, 2004, **70**, 174113.
45. E. A. Brandes and G. B. Brook, *Smithells Metals Reference Book, 7th ed*, Butterworth-Heinemann, Oxford, 1992.
46. Y. Li, S. Y. Luo, J. H. Li, J. B. Liu and B. X. Liu, *J. Mater. Sci.*, 2014, **49**, 7263-7272.
47. Q. Zhang, W. S. Lai and B. X. Liu, *J. Comput-Aided Mater.*, 1999, **6**, 103-116.
48. J. H. Rose, J. R. Smith, F. Guinea and J. Ferrante, *Phys. Rev. B*, 1984, **29**, 2963-2969.
49. *See http://lammps.sandia.gov for LAMMPS package*.
50. S. Y. Luo, J. H. Li, J. B. Liu and B. X. Liu, *Acta Mater.*, 2014, **76**, 482-492.
51. C. Suryanarayana and M. G. Norton, *X-ray diffraction: a practical approach*, Plenum Press, New York, 1998.
52. J. L. Finney, *Proc. Roy. Soc. Lond. A*, 1970, **319**, 479-493.
53. M. H. Yang, N. Li, J. H. Li and B. X. Liu, *J. Alloys Compd.*, 2014, **606**, 7-10.
54. Z. J. Zhang and B. X. Liu, *J. Appl. Phys.*, 1994, **76**, 3351.
55. A. W. Weeber and H. Bakker, *J. Phys. F: Met. Phys.*, 1988, **18**, 1359-1369.
56. F. Li, X. J. Liu and Z. P. Lu, *Comp. Mater. Sci.*, 2014, **85**, 147-153.
57. S. Q. Wu, C. Z. Wang, S. G. Hao, Z. Z. Zhu and K. M. Ho, *Appl. Phys. Lett.*, 2010, **97**, 21901.
58. P. F. Guan, T. Fujita, A. Hirata, Y. H. Liu and M. W. Chen, *Phys. Rev. Lett.*, 2012, **108**, 175501.
59. J. Zemp, M. Celino, B. Sch Nfeld and J. F. L Ffler, *Phys. Rev. B*, 2014, **90**, 144108.
60. R. Soklaski, Z. Nussinov, Z. Markow, K. F. Kelton and L. Yang, *Phys. Rev. B*, 2013, **87**, 184203.
61. Q. Wang, J. H. Li, J. B. Liu and B. X. Liu, *Phys. Chem. Chem. Phys.*, 2014, **16**, 19590.
62. Y. Q. Cheng and E. Ma, *Prog. Mater. Sci.*, 2011, **56**, 379-473.
63. M. H. Yang, J. H. Li and B. X. Liu, *RSC Adv.*, 2015, **5**, 16400-16404.
64. X. K. Xi, L. L. Li, B. Zhang, W. H. Wang and Y. Wu, *Phys. Rev. Lett.*, 2007, **99**, 95501.
65. D. R. Nelson and F. Spaepen, *Solid State Phys.*, 1989, **42**, 1-90.
66. Y. Q. Cheng, E. Ma and H. W. Sheng, *Phys. Rev. Lett.*, 2009, **102**, 245501.
67. D. Xu, G. Duan and W. L. Johnson, *Phys. Rev. Lett.*, 2004, **92**, 245504.
68. L. Xia, S. S. Fang, Q. Wang, Y. D. Dong and C. T. Liu, *Appl. Phys. Lett.*, 2006, **75**, 171905.

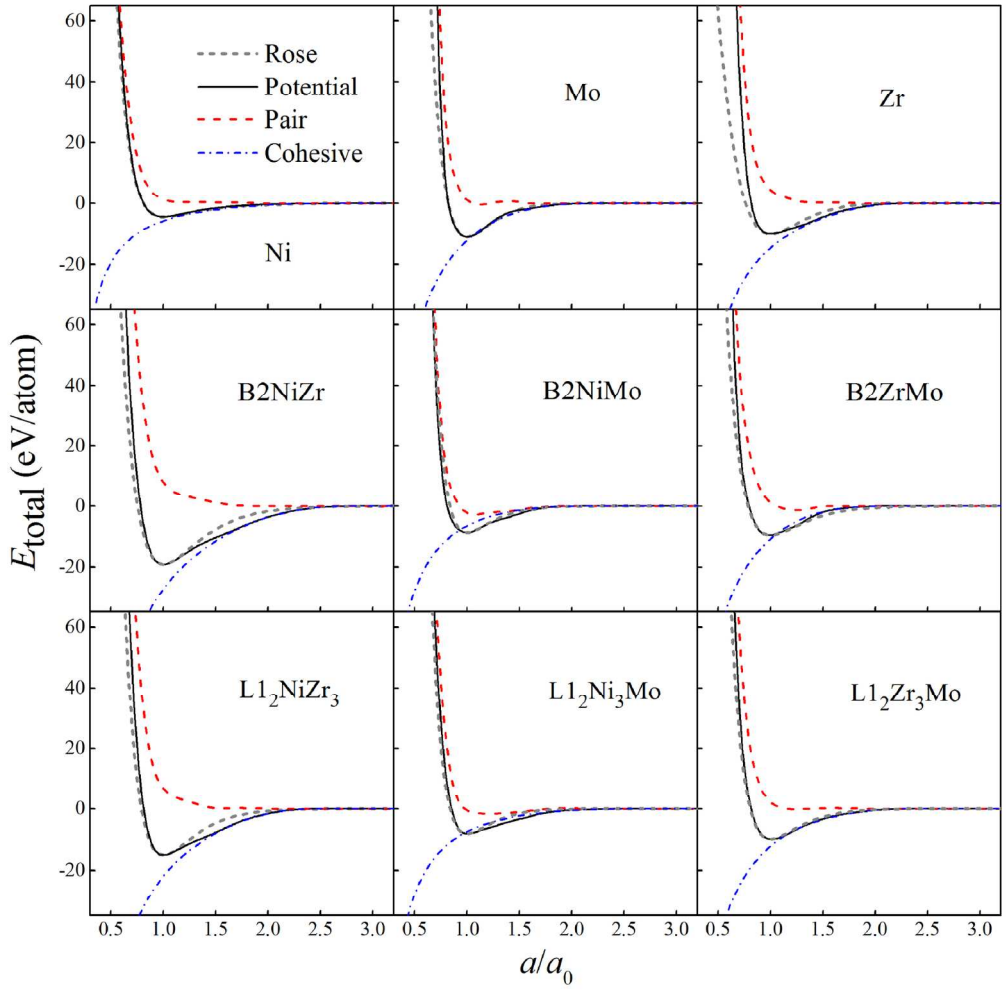

Figure1
80x80mm (600 x 600 DPI)

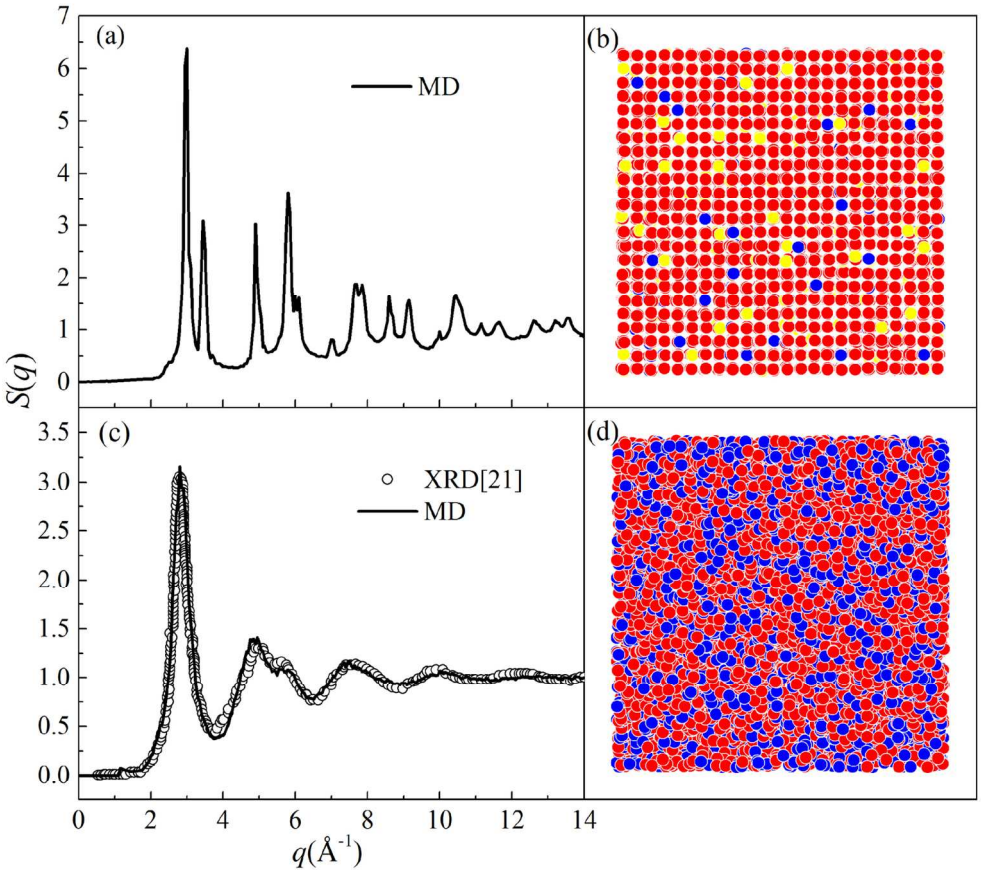

Figure2
69x61mm (600 x 600 DPI)

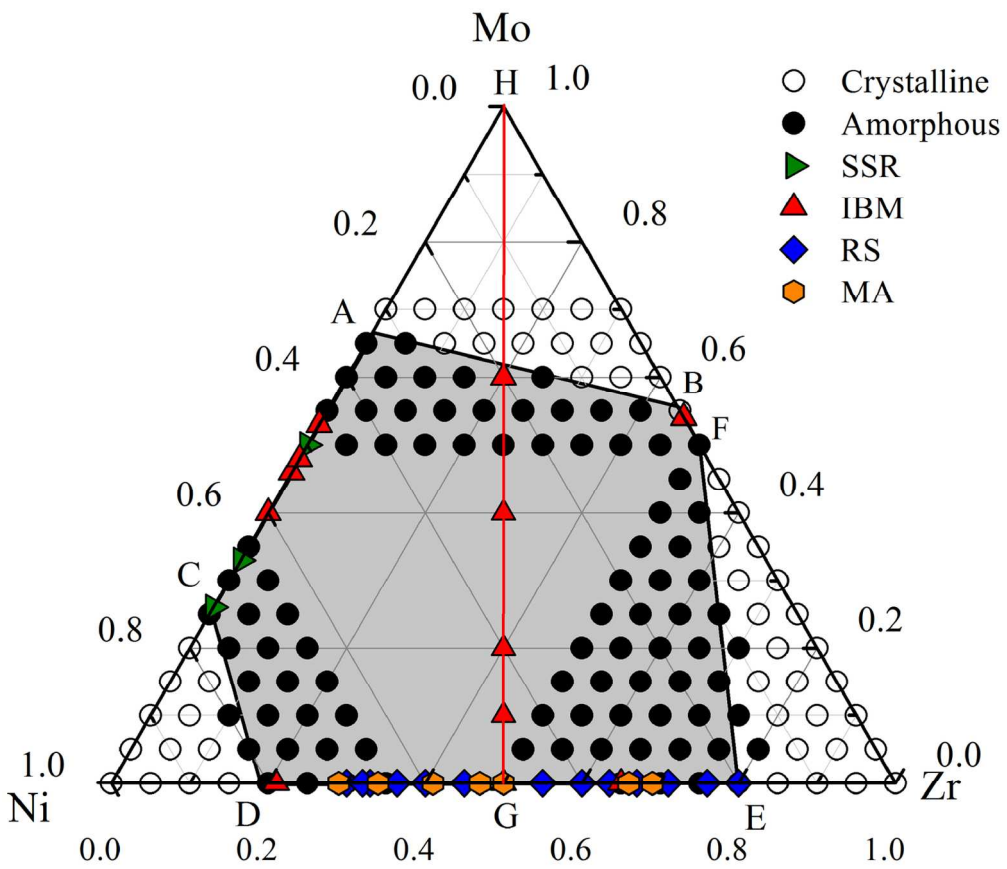

Figure3
69x61mm (600 x 600 DPI)

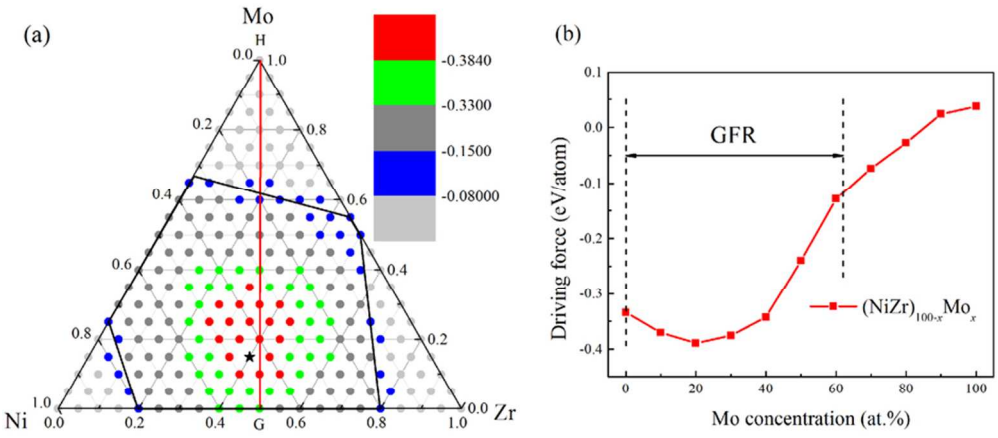

Figure4
40x20mm (600 x 600 DPI)

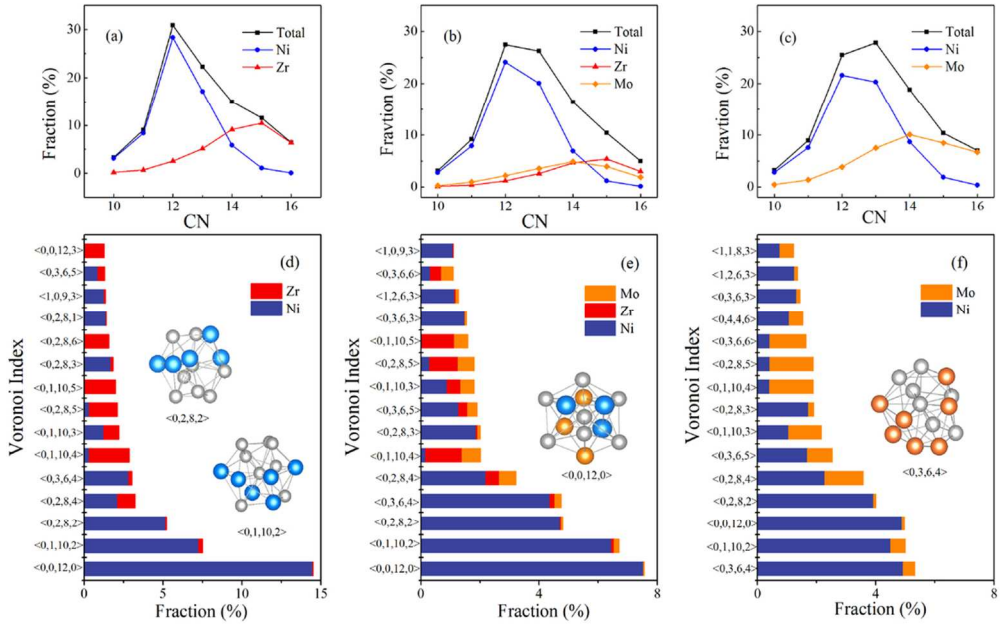

Figure5
49x31mm (600 x 600 DPI)

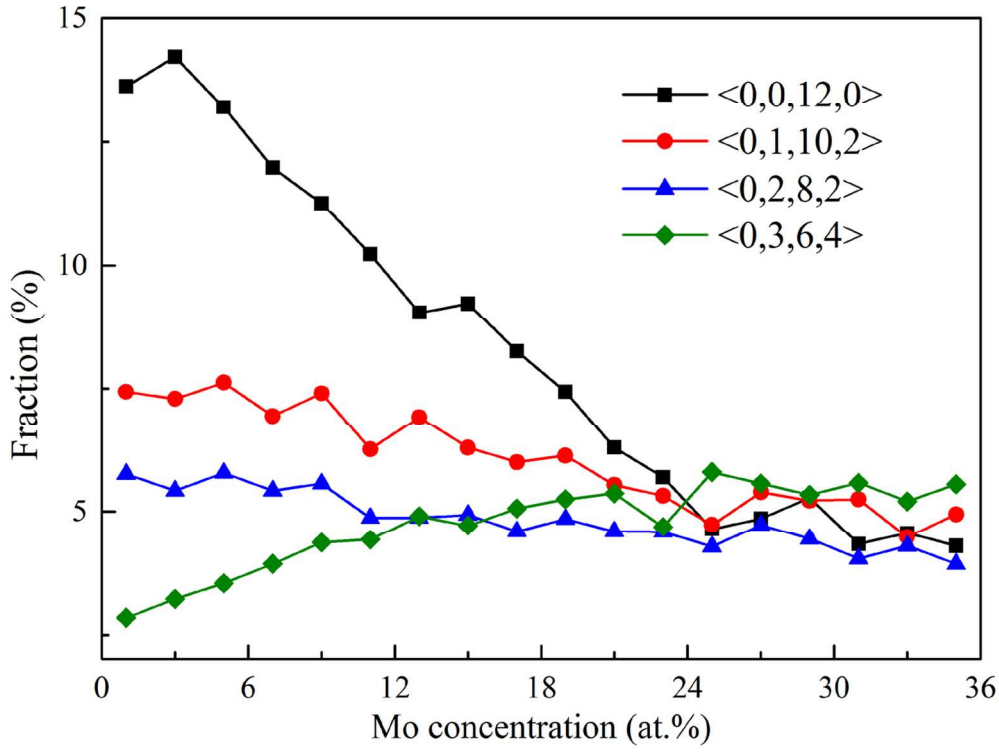

Figure6
59x45mm (600 x 600 DPI)

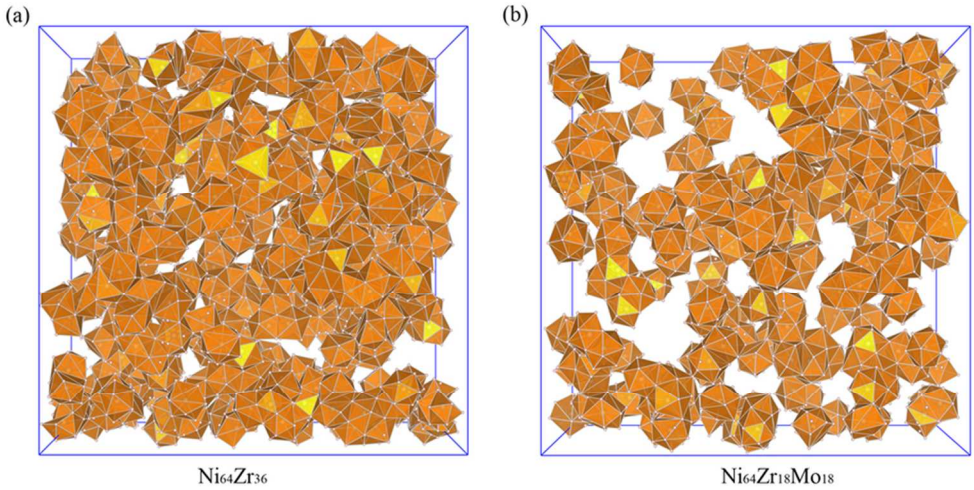

Figure7
40x20mm (600 x 600 DPI)

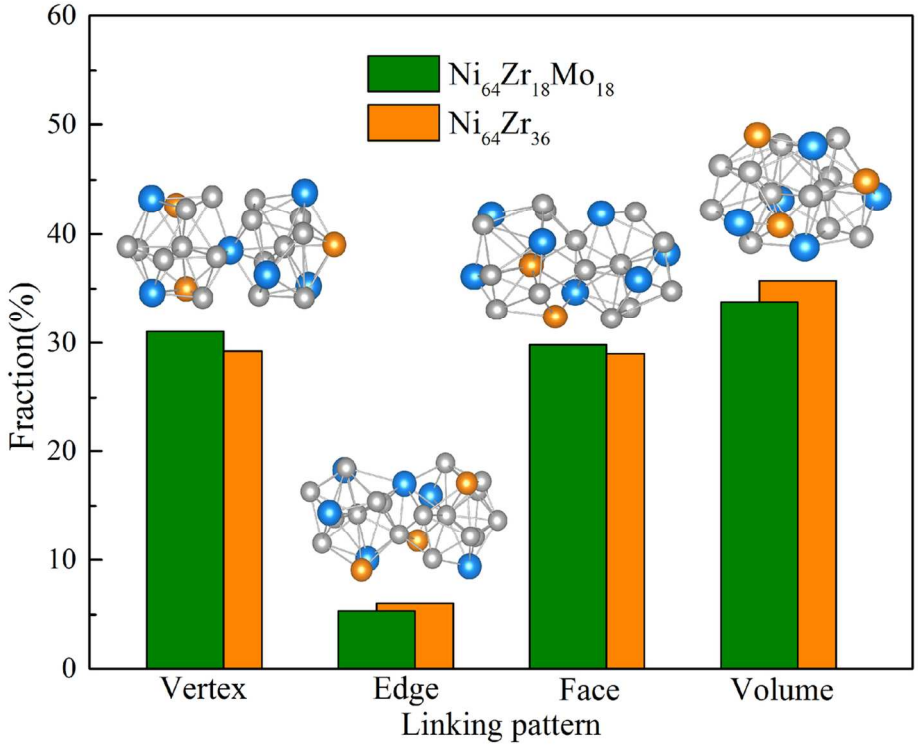

Figure8
59x45mm (600 x 600 DPI)

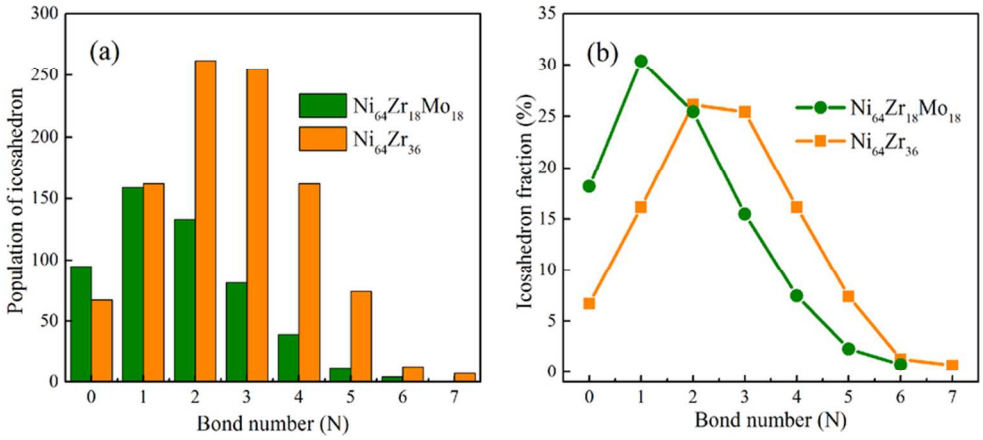

Figure9
40x20mm (600 x 600 DPI)

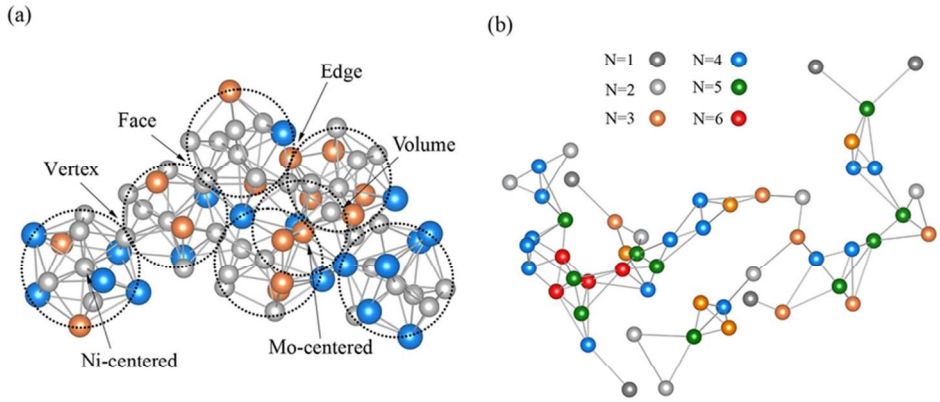

Figure10
40x20mm (600 x 600 DPI)